Advances in Applied Mathematics and Mechanics
Adv. Appl. Math. Mech., Vol. **16**, No. 2, pp. 493-518

DOI: 10.4208/aamm.OA-2022-0237
April 2024

Nonconforming Finite Element Methods for Two-Dimensional Linearly Elastic Shallow Shell Model

Rongfang Wu[1], Xiaoqin Shen[2,3,*], Dongyang Shi[4] and Jiaping Yu[5]

[1] *School of Computer Science and Engineering, Xi'an University of Technology, Xi'an, Shaanxi 710048, China*
[2] *School of Sciences, Xi'an University of Technology, Xi'an, Shaanxi 710054, China*
[3] *State Key Laboratory of Eco-hydraulics in Northwest Arid Region, Xi'an, Shaanxi 710048, China*
[4] *School of Mathematics and Statistics, Zhengzhou University, Zhengzhou, Henan 450001, China*
[5] *College of Science, Donghua University, Shanghai 201620, China*

Received 8 September 2022; Accepted (in revised version) 20 November 2022

Abstract. A shell whose height is far less than the minimum size covering the bottom is called the shallow shell. As a branch of linear elastic shell, it is a special shell with large span and has been widely applied in engineering fields. The main aim of this paper is to construct a general nonconforming finite element framework for a two-dimensional shallow shell model proposed by Ciarlet and Miara. Based on the different regularities of the displacement components, we give the special properties satisfied by the general framework and provide several nonconforming finite element discretization schemes. Then, the existence and uniqueness of the numerical solutions are proved, with the rate of convergence derived. Finally, numerical experiments are carried out for the paraboloid, spherical dome and cylindrical bridge, which validates the theoretical analyses. Moreover, the computing cost of discretizing the shallow shell model is evidently less than that of discretizing the general shell model with comparable accuracy when the shell is the large span shell.

AMS subject classifications: 65N12, 65N15, 65N30

Key words: Shallow shell, nonconforming FEMs, numerical analysis.

*Corresponding author.
Email: xqshen@xaut.edu.cn (X. Shen)

1 Introduction

The linearly elastic shallow shell, a branch of the linearly elastic shell, is an important topic in elastic theory. Shallow shells are frequently used in many engineering fields, such as the roof, gymnasium, arch bridge, just name a few of them. The *locking phenomena* [1, 2], i.e., the numerical solution approaches to zero whereas the true solution does not approaches to zero when the semi-thickness ε of the shell approximates to zero, can be observed frequently in discretization of the three-dimensional (3D) model. In order to avoid this phenomenon, the two-dimensional (2D) model has attracted increasing attention recently. Using the asymptotical analysis, Ciarlet and Miara [3] proved that, as the thickness of the shell approaches zero, the solution of the 2D shallow shell equation is the H^1-limit of the solutions of scaled 3D equation. Léger and Miara [4] studied the shallow shells with single-sided contact of obstacles. Raja and Sabu [5] deduced that when the thickness of material tends to zero, the minimized energy function sequence of the 3D shallow shell model converges to the minimized energy function sequence related to the 2D model by Γ-convergence method.

For the numerical analyses, [6–8] used the conforming finite element discretization for the classical shell model and proved the error estimates. In a recent paper, we have carried out conforming element discretization for shallow shell model [9]. As we all know, one drawback of conforming element approximation is that the number of the degrees of freedom is very large and the degrees of the shape function are usually quite high. Compared with the conforming finite elements, the nonconforming element [10,11] employs fewer degrees of freedom.

The main purpose of the present work is to design efficient nonconforming finite element methods, and investigate the properties of the approximating solution. Motivated by the different smoothness of the displacement components, the conforming finite element (e.g., linear or bilinear elements) is used to approximate the first two components of the displacement, whereas the nonconforming finite element (e.g., Morley, Zienkiewicz, Fraeijs de Veubeke, Specht, rectangular Morley and ACM elements) is used to approximate the third component. It seems interesting to approximate different component of a vector field by different finite elements. Such idea has been used in problems arising from the shell model [12], Stokes flow [13], Reissner-Mindlin plate [14] and Maxwell equations [15]. Moreover, we prove that these numerical schemes have the same rate of convergence in the energy norm. It is worth mentioning that the discretization cost of shallow shell model is obviously lower than that of the Koiter's shell with comparable accuracy, which may be due to the different coordinate systems employed in these two types of models.

The rest of this paper is organized as follows. In Section 2, we prove the existence and the uniqueness of the weak solution of the 2D shallow shell model. In Section 3, we propose several finite element schemes to approximate the displacement field, and a discussion on the well-posedness of the numerical solution, and derive the error estimates for all the schemes. In Section 4, the Morley element is employed as the representative to

examine the efficiency and the validity of the theoretical results.

2 2D linearly elastic shallow shell model

Our notations are mostly borrowed from [16]. Let $\omega \subset \mathbb{R}^2$ be a bounded open connected subset and its boundary $\gamma = \partial\omega$ is Lipschitz-continuous with a clamped boundary $\gamma_0 \subset \gamma$ with $\text{meas}(\gamma_0) > 0$, noting that ω is locally on one side of γ.

Let $z(x,y)$ represent the equation of the middle surface of the shell. If it holds:

$$\left(\frac{dz}{dx}\right)^2 \ll 1, \quad \left(\frac{dz}{dy}\right)^2 \ll 1,$$

then the shell is called a shallow shell. In other words, the shallow shell has a relatively small rise as compared to its spans (see Fig. 1).

Define the spaces

$$\vec{V}_H(\omega) = \left\{ \vec{\eta}_H = (\eta_1, \eta_2) \in H^1(\omega) \times H^1(\omega);\ \vec{\eta}_H = \vec{0} \text{ on } \gamma_0 \right\}$$

and

$$V_3(\omega) = \left\{ \eta_3 \in H^2(\omega);\ \eta_3 = \partial_\nu \eta_3 = 0 \text{ on } \gamma_0 \right\}.$$

Let $\theta(x_1, x_2)$ denote the displacement of the point (x_1, x_2) in the middle surface. $\partial_\alpha = \partial/\partial x_\alpha$, $\partial_{\alpha\beta} = \partial/\partial x_\alpha \partial x_\beta$, δ_{ij}, Δ and ∇ denote the Kronecker symbol, Laplace operator and gradient operator, respectively.

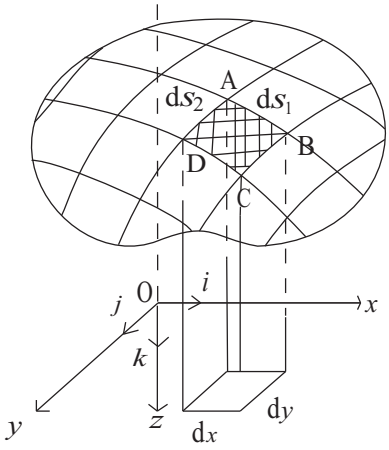

Figure 1: Shallow shell: $z(x,y)$ represents the equation of the shell middle surface (cf. [17]).

Problem 2.1. Assume that $f_i \in L^2(\omega\times(-1,1))$, $g_i \in L^2(\omega\times\{1\}\bigcup\omega\times\{-1\})$, $\theta\in\mathcal{C}^3(\overline{\omega})$. The function $\vec{\zeta}=(\zeta_\alpha,\zeta_3)\in \vec{V}_H(\omega)\times V_3(\omega)$ solves the following variational system for any $\eta_3\in V_3(\omega)$, $\eta_\alpha\in\vec{V}_H(\omega)$

$$\begin{cases} -\displaystyle\int_\omega m_{\alpha\beta}\partial_{\alpha\beta}\eta_3 d\omega+\int_\omega n^\theta_{\alpha\beta}\partial_\alpha\theta\partial_\beta\eta_3 d\omega=\int_\omega p_3\eta_3 d\omega-\int_\omega s_\alpha\partial_\alpha\eta_3 d\omega, \\ \displaystyle\int_\omega n^\theta_{\alpha\beta}\partial_\beta\eta_\alpha d\omega=\int_\omega p_\alpha\eta_\alpha d\omega, \end{cases} \tag{2.1}$$

where $m_{\alpha\beta}\partial_{\alpha\beta}$ $(\alpha,\beta=1,2)$ denotes a summation convention,

$$\begin{aligned} m_{\alpha\beta}&=-\left\{\frac{4\lambda\mu}{3(\lambda+2\mu)}\Delta\zeta_3\delta_{\alpha\beta}+\frac{4}{3}\mu\partial_{\alpha\beta}\zeta_3\right\}, \\ n^\theta_{\alpha\beta}&=\frac{4\lambda\mu}{\lambda+2\mu}e^\theta_{\rho\rho}(\vec{\zeta})\delta_{\alpha\beta}+4\mu e^\theta_{\alpha\beta}(\vec{\zeta}), \\ e^\theta_{\alpha\beta}(\vec{\zeta})&=\frac{1}{2}(\partial_\alpha\zeta_\beta+\partial_\beta\zeta_\alpha+\partial_\alpha\theta\partial_\beta\zeta_3+\partial_\beta\theta\partial_\alpha\zeta_3), \\ p_i&=\int_{-1}^1 f_i dy_3+g_i^++g_i^-, \\ s_\alpha&=\int_{-1}^1 y_3 f_\alpha dy_3+g_\alpha^+-g_\alpha^-. \end{aligned}$$

Theorem 2.1 (Existence and uniqueness of the weak solution)**.** *Let $\omega\subset\mathbb{R}^2$ be a bounded open connected subset, where the boundary $\gamma=\partial\omega$ is Lipschitz-continuous. Assume that γ_0 is a non-empty open subset of γ, $f_i\in L^2(\omega\times(-1,1))$, $g_i\in L^2(\omega\times\{1\}\bigcup\omega\times\{-1\})$ and $\theta\in\mathcal{C}^3(\overline{\omega})$ are functions independent of semi-thickness ε. Then, the system* (2.1) *has a unique solution.*

Proof. We define the bilinear operator $B(\cdot,\cdot)$ and linear function $f(\cdot)$ as

$$\begin{aligned} B(\vec{\zeta},\vec{\eta})&=\int_\omega\frac{4\lambda\mu}{\lambda+2\mu}\left(\frac{1}{3}(\Delta\zeta_3)(\Delta\eta_3)+e^\theta_{\alpha\alpha}(\vec{\zeta})e^\theta_{\beta\beta}(\vec{\eta})\right)d\omega \\ &\quad+\int_\omega 4\mu\left(\frac{1}{3}\partial_{\alpha\beta}(\zeta_3)\partial_{\alpha\beta}(\eta_3)+e^\theta_{\alpha\beta}(\vec{\zeta})e^\theta_{\alpha\beta}(\vec{\eta})\right)d\omega, \\ f(\vec{\eta})&:=\int_\omega(p_i\eta_i-s_\alpha\partial_\alpha\eta_3)d\omega, \end{aligned}$$

respectively. Then, the system (2.1) can be rewritten as: Find

$$\vec{\zeta}\in\vec{V}(\omega)=\vec{V}_H(\omega)\times V_3(\omega)=\{\vec{\zeta}=(\zeta_i)\in H^1(\omega)\times H^1(\omega)\times H^2(\omega);\ \zeta_i=\partial_\nu\zeta_3=0 \text{ on } \gamma_0\},$$

such that

$$B(\vec{\zeta},\vec{\eta})=f(\vec{\eta}),\quad \forall\vec{\eta}\in\vec{V}(\omega). \tag{2.2}$$

We define the semi-norms on space $\vec{V}(\omega)$ as:

$$|\eta_\beta|_{1,\omega}=\left\{\sum_\alpha|\partial_\alpha\eta_\beta|^2_{0,\omega}\right\}^{1/2}\quad \text{for } \beta=1,2,$$

and

$$|\eta_3|_{2,\omega}=\left\{\sum_{\alpha,\beta}|\partial_{\alpha\beta}\eta_3|^2_{0,\omega}\right\}^{1/2},$$

respectively. It is easy to see that they are equivalent to the norms $\|\cdot\|_{1,\omega}$ and $\|\cdot\|_{2,\omega}$ over the space $\vec{V}(\omega)$ respectively. Then the bilinear form $B(\cdot,\cdot)$ is $\vec{V}(\omega)-$ elliptic (cf. Theorem 3.6.1 of [18]). By means of the Lax-Milgram theorem (cf. e.g., [19]), it is guaranteed that the variational problem (2.2) has a unique solution. □

3 Numerical method

Based on the different regularities of the three components of displacement vector field, we adopt two types of conforming elements to approximate the first two components ζ_α of the unknown vector field of displacement, and six types of the nonconforming elements to approximate the third component ζ_3.

To go into detail, let $\bar{\omega}$ be a polygon domain, $\mathcal{T}_h$ be a shape regular partitions of $\bar{\omega}$ with triangles or rectangles. For a given $T\in\mathcal{T}_h$, let

$$h_T=diam(T),\quad h=\max_{T\in\mathcal{T}_h}h_T\quad \text{and}\quad \rho_T=\underset{S\subset T}{superior diam}(S),$$

S is a ball contained in T. Throughout this paper, we assume:

H1. There are at least two continuous points on the common edge of adjacent element;

H2. The partition $\mathcal{T}_h$ satisfies the inverse assumption ($h/h_T\leq C$, $\forall T\in\mathcal{T}_h$, C denotes a positive constant independent of h) and the quasi uniform assumption ($h_T/\rho_T\leq C$, $\forall T\in\mathcal{T}_h$) [20–22].

Next, we can use the following six schemes to discretize the displacement in the finite element space $\vec{V}_h:=V_{1h}\times V_{2h}\times V_{h3}$, where $V_{\alpha h}$ $(\alpha=1,2)$ represents the space of the conforming linear and bilinear elements, and V_{h3} represents the space of the nonconforming Morley, Zienkiewicz, Fraeijs de Veubeke, Specht, rectangular Morley and ACM elements.

Scheme 3.1 (Linear/Morley element pair)**.** The linear element space is defined by

$$V^P_{\alpha h}:=\{\eta_h\in C^0(\omega):\eta_h|_T\in P_1(T)\text{ for each }T\in\mathcal{T}_h,\ \eta_h=0\text{ on }\gamma_0\},\quad \alpha=1,2.$$

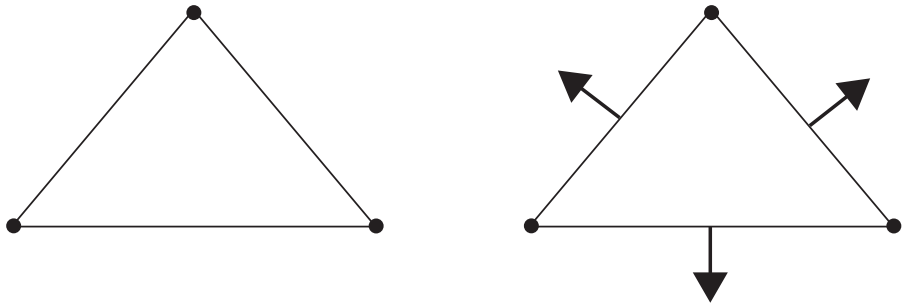

Figure 2: (a) Linear element; (b) Morley element. •: Vertex, →: The normal derivative of midpoint.

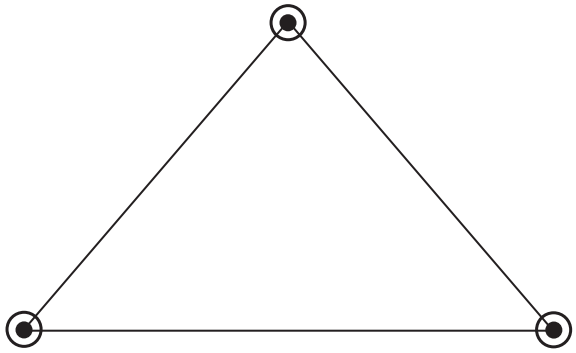

Figure 3: Zienkiewicz element. ◯: The first partial derivative.

The Morley element space [23,24] is defined by

$$\begin{aligned} V_{3h}^{M} := \{ & \eta_h \in L^2(\omega) : \eta_h|_T \in P_2(T) \text{ for each } T \in \mathcal{T}_h; \\ & \eta_h \text{ is continuous at each interior vertex } a_i, \ (i=1,2,3), \\ & \partial_v \eta_h \text{ is continuous at mid-point of the interior edge } K, \\ & \eta_h(a_i) = \partial_v \eta_h(a_{ij}) = 0, \ 1 \le i < j \le 3, \text{ for } a_i \in \gamma_0 \}, \end{aligned}$$

where

$$a_{ij} = \frac{1}{2}(a_i + a_j).$$

Scheme 3.2 (Linear/Zienkiewicz element pair)**.** The Zienkiewicz element space [25] is

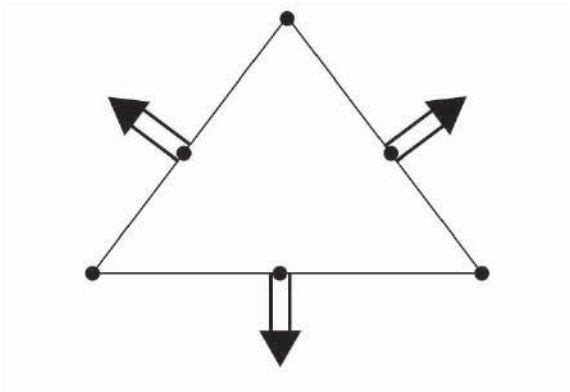

Figure 4: Fraeijs de Veubeke element. ⇒: The mean value of the normal derivative along each edge.

defined by

$$\begin{aligned} V_{3h}^{Z} := \Big\{ & \eta_h \in L^2(\omega) : \eta_h\Big|_T \in P_3(T) \text{ for each } T \in \mathcal{T}_h; \\ & \eta_h, \frac{\partial \eta_h}{\partial x_1} \text{ and } \frac{\partial \eta_h}{\partial x_2} \text{ are continuous at each interior vertex } a_i, \\ & \eta_h(a_i) = \frac{\partial \eta_h}{\partial x_1}(a_i) = \frac{\partial \eta_h}{\partial x_2}(a_i) = 0 \text{ for } a_i \in \gamma_0, \\ & \eta_h \text{ on each } T \text{ satisfies function } \phi(\eta_h) = 0 \Big\}, \end{aligned}$$

where

$$\phi(\eta_h) = 6\eta_h(a_0) - 2\sum_{i=1}^{3}\eta_h(a_i) + \sum_{i=1}^{3}(a_i - a_0)\cdot\nabla\eta_h(a_i), \quad a_0 = \frac{1}{3}\sum_{i=1}^{3}a_i.$$

Scheme 3.3 (Linear/Fraeijs de Veubeke element pair)**.** The Fraeijs de Veubeke element space [23,26] is defined by

$$\begin{aligned} V_{3h}^{F} := \Big\{ & \eta_h \in L^2(\omega) : \eta_h\Big|_T \in P_3(T) \text{ for each } T \in \mathcal{T}_h; \\ & \eta_h \text{ is continuous at each interior vertex } a_i, \\ & \eta_h \text{ is continuous at mid-point of the edge } K_i, \\ & \eta_h(a_i) = \eta_h(a_{ij}) = 0,\ 1 \le i < j \le 3,\ \frac{1}{|K_i|}\int_{K_i}\partial_\nu \eta_h ds \text{ for } a_i, K_i \in \gamma_0, \\ & \eta_h \text{ on each } T \text{ satisfies function } \varphi(\eta_h) = 0 \Big\}, \end{aligned}$$

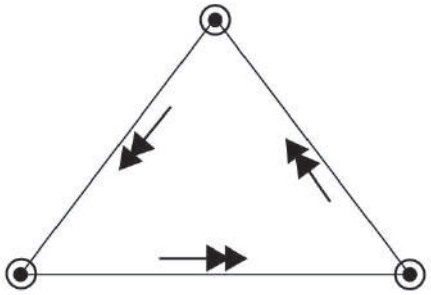

Figure 5: Specht element. ↠: The moment of the normal derivative along each edge.

where

$$\varphi(\eta_h)=27\eta_h(a_0)-\sum_{i=1}^{3}\eta_h(a_i)-8\sum_{i=1}^{3}\eta_h(a_{ij})+3\sum_{i=1}^{3}\frac{1}{|K_i|}\int_{K_i}\nabla\eta_h\cdot(a_i-a_0)ds,$$
$$a_{ij}=\frac{1}{2}(a_i+a_j),\quad a_0=\frac{1}{3}\sum_{i=1}^{3}a_i.$$

Scheme 3.4 (Linear/Specht element pair)**.** The Specht element space [27, 28] is defined by

$$\begin{aligned}V_{3h}^{S}:=\Big\{&\eta_h\in L^2(\omega):\eta_h\Big|_T\in\{Z_3(T)+b_k\mathbb{P}_2(T)\}\text{ for each }T\in\mathcal{T}_h;\\&\eta_h,\ \frac{\partial\eta_h}{\partial x_1}\text{ and }\frac{\partial\eta_h}{\partial x_2}\text{ are continuous at each interior vertex }a_i,\\&\eta_h(a_i)=\frac{\partial\eta_h}{\partial x_1}(a_i)=\frac{\partial\eta_h}{\partial x_2}(a_i)=0\text{ for }a_i\in\gamma_0,\\&\eta_h\text{ on each }T\text{ satisfies function }\psi(\eta_h)=0\Big\},\end{aligned}$$

where $Z_3(T)$, b_k and $\mathbb{P}_2$ denote the Zienkiewicz space, cubic bubble function and the second order Legendre polynomial,

$$\psi(\eta_h)=\int_{K_i}\mathbb{P}_2\partial_\nu\eta_h ds.$$

Scheme 3.5 (Bilinear/Rectangular Morley element pair)**.** The bilinear element space is defined by

$$V_{\alpha h}^{RP}:=\{\eta_h\in C^0(\omega):\eta_h|_T\in P_1(T)\oplus\{x_1x_2\}\text{ for each }T\in\mathcal{T}_h,\ \eta_h=0\text{ on }\gamma_0\}.$$

Figure 6: (a) Bilinear element; (b) Rectangular Morley element.

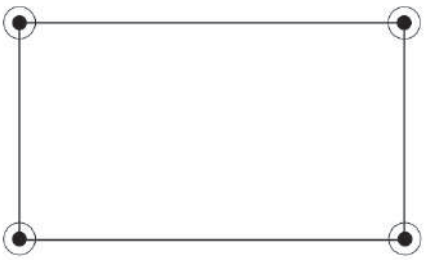

Figure 7: ACM element.

The rectangular Morley element space [29,30] is defined by

$$V_{3h}^{RM}:=\Big\{\eta_h\in L^2(\omega):\eta_h\Big|_T\in P_2(T)\oplus\{x_1^3,x_2^3\}\text{ for each }T\in\mathcal{T}_h;\\ \eta_h\text{ is continuous at each interior vertex }a_i\ (i=1,2,3,4),\\ \partial_\nu\eta_h\text{ is continuous at the mid-point of the interior edge }K,\\ \eta_h(a_i)=\partial_\nu\eta_h(a_{ij})=0,\ 1\le i<j\le 4,\ j-i\neq 2\text{ for }a_i\in\gamma_0\Big\},$$

where

$$a_{ij}=\frac{1}{2}(a_i+a_j).$$

Scheme 3.6 (Bilinear/ACM element pair)**.** The ACM element space [31] is defined by

$$V_{3h}^{A}:=\Big\{\eta_h\in L^2(\omega):\eta_h\Big|_T\in P_3(T)\oplus\{x_1^3x_2,x_1x_2^3\}\text{ for each }T\in\mathcal{T}_h;\\ \eta_h,\ \frac{\partial\eta_h}{\partial x_1}\text{ and }\frac{\partial\eta_h}{\partial x_2}\text{ are continuous at each interior vertex }a_i,\\ \eta_h(a_i)=\frac{\partial\eta_h}{\partial x_1}(a_i)=\frac{\partial\eta_h}{\partial x_2}(a_i)=0,\ i=1,2,3,4,\text{ for }a_i\in\gamma_0\Big\}.$$

For the above-mentioned Morley, Zienkiewicz, Fraeijs de Veubeke, Specht, rectangular Morley and ACM elements, $P_k(T)$, $k\geq 1$, is the polynomial space of degree equal to or less than k on T. Then, we set the following conditions:

C1) $\forall w_{3h}\in V_{h3}$, w_{3h} is continuous at the vertices of T and is zero at the vertices on γ_0;

C2) $\forall w_{3h}\in V_{h3}$, $\partial_\beta w_{3h}$ is continuous at the vertices of T and is zero at the vertices on γ_0;

C3) $\forall w_{3h}\in V_{h3}$, $\int_F w_{3h}ds$ is continuous across the element common edge F and is zero on $F\in\gamma_0$;

C4) $\forall w_{3h}\in V_{h3}$, $\int_F \frac{\partial w_{3h}}{\partial \nu}ds$ is continuous at midpoints of the interior edge and is zero at midpoints of the boundary edge γ_0;

C5) Let $\Pi_h w_{3h}\in V_{h3}$ be the finite element interpolation of w_{3h},

$$\|w_{3h}-\Pi_h w_{3h}\|_h\leq Ch\|w_{3h}\|_3,\quad \forall w_{3h}\in H^2(\omega)\cap H^3(\omega),$$

where

$$\|\cdot\|_h=\Big(\sum_{T\in\mathcal{T}_h}|\cdot|_{2,T}^2\Big)^{1/2}.$$

Then the approximation of variational problem (2.2) is to find $\vec{\zeta}_h\in\vec{V}_h$ such that

$$B_h(\vec{\zeta}_h,\vec{\eta}_h)=f(\vec{\eta}_h),\quad \forall\vec{\eta}_h\in\vec{V}_h, \tag{3.1}$$

where

$$B_h(\vec{\zeta}_h,\vec{\eta}_h)=-\sum_{T\in\mathcal{T}_h}\int_T m_{\alpha\beta}\partial_{\alpha\beta}\eta_{3h}dx+\sum_{T\in\mathcal{T}_h}\int_T n^\theta_{\alpha\beta}\partial_\alpha\theta\partial_\beta\eta_{3h}dx+\sum_{T\in\mathcal{T}_h}\int_T n^\theta_{\alpha\beta}\partial_\beta\eta_{\alpha h}dx. \tag{3.2}$$

We define the norm on $\vec{V}_h$ as: for $\vec{\eta}_h=(\eta_{1h},\eta_{2h},\eta_{3h})\in\vec{V}_h$,

$$\|\vec{\eta}_h\|:=\sum_\alpha\|\eta_{\alpha h}\|_{H^1(\omega)}+||\eta_{3h}\|_h.$$

Lemma 3.1 (Continuity and coercivity)**.** *Let $\vec{V}_h$ be the discrete space, then there exist positive constants α_0 and α_1, such that*

$$|B_h(\vec{\zeta}_h,\vec{\eta}_h)|\leq\alpha_1\|\vec{\zeta}_h\|\|\vec{\eta}_h\|,\qquad \forall\vec{\zeta}_h,\ \vec{\eta}_h\in\vec{V}_h, \tag{3.3a}$$

$$B_h(\vec{\eta}_h,\vec{\eta}_h)\geq\alpha_0\|\vec{\eta}_h\|^2,\qquad \forall\vec{\eta}_h\in\vec{V}_h. \tag{3.3b}$$

Proof. Note that $\sqrt{B_h(\cdot,\cdot)}$ is equivalent to the norm $||\cdot||$ on space $\vec{V}_h$. From the Cauchy-Schwarz inequality, it is clear that (3.3a) holds true.

On the other hand, for each element $T\in\mathcal{T}_h$, applying (3.2) and the generalized patch test [32]

$$\lim_{h\to 0}\sup_{\vec{\eta}_h\in\vec{V}_h}\left|\sum_{T\in\mathcal{T}_h}\int_{\partial T}\phi\partial^{\alpha}\vec{\eta}_h\nu_i ds\right|=0,\quad 1\le i\le 2,\quad |\alpha|<2,\quad \phi\in C_0^{\infty},\quad \vec{\eta}_h\in\vec{V}_h,$$

yields

$$\begin{aligned}B_h(\vec{\eta}_h,\vec{\eta}_h)=&\sum_{T\in\mathcal{T}_h}\int_T\left\{\frac{4\lambda\mu}{\lambda+2\mu}\left(\frac{1}{3}(\Delta\eta_{3h})^2+(e^{\theta}_{\alpha\alpha}(\vec{\eta}_h))^2\right)\right\}dx\\&+\sum_{T\in\mathcal{T}_h}\int_T\left\{4\mu\left(\frac{1}{3}(\partial_{\alpha\beta}(\eta_{3h}))^2+(e^{\theta}_{\alpha\beta}(\vec{\eta}_h))^2\right)\right\}dx\\\ge&4\mu\sum_{T\in\mathcal{T}_h}\int_T\left\{\frac{1}{3}(\partial_{\alpha\beta}(\eta_{3h}))^2+(e^{\theta}_{\alpha\beta}(\vec{\eta}_h))^2\right\}dx\\\ge&C\sum_{T\in\mathcal{T}_h}\left(\sum_{\alpha,\beta}|\partial_{\alpha\beta}\eta_{3h}|^2_{0,T}+\sum_{\alpha,\beta}|(e^{\theta}_{\alpha\beta}(\vec{\eta}_h))|^2_{0,T}\right).\end{aligned}$$

When nonconforming finite element space satisfies the conditions described in **H1** and **H2**, we could know by the generalized Korn's inequality [18, 33–35], that there exists a constant $L>0$ independent of h such that

$$\sum_{\alpha,\beta}|e^{\theta}_{\alpha\beta}(\vec{\eta}_h)|^2_{0,\omega}\ge L\sum_{\alpha,\beta}|\partial_{\alpha}\eta_{\beta h}|^2_{0,\omega}.$$

Therefore, $\forall\vec{\eta}_h\in\vec{V}_h$, and we have

$$\begin{aligned}B_h(\vec{\eta}_h,\vec{\eta}_h)\ge&C\sum_{T\in\mathcal{T}_h}\left(\sum_{\alpha,\beta}|\partial_{\alpha\beta}\eta_{3h}|^2_{0,T}+\sum_{\alpha,\beta}|(e^{\theta}_{\alpha\beta}(\vec{\eta}_h))|^2_{0,T}\right)\\\ge&\alpha_0\sum_{T\in\mathcal{T}_h}\left(\sum_{\beta}|\eta_{\beta h}|^2_{1,T}+|\eta_{3h}|^2_{2,T}\right)\ge\alpha_0\|\vec{\eta}_h\|^2,\end{aligned}$$

which is the desired result of (3.3b). The proof is completed. □

Lemma 3.2 (Error estimate). *Let $\vec{\zeta}$ and $\vec{\zeta}_h$ be the solutions of* (2.2) *and* (3.1) *respectively. Then there exists a constant $C>0$ independent of h such that for the space V_{h3} (V_{h3} indicates V^M_{3h}, V^Z_{3h}, V^F_{3h}, V^S_{3h}, V^{RM}_{3h} and V^A_{3h}, respectively), it holds*

$$\|\zeta_3-\zeta_{3h}\|_h\le C\left(\inf_{\zeta_{3h}\in V_{h3}}\|\zeta_3-\eta_{3h}\|_h+\sup_{w_{3h}\in V_{h3}}\frac{|E_h(\zeta_3,w_{h3})|}{\|w_{3h}\|_h}\right),\tag{3.4}$$

where

$$E_h(\zeta_3,w_{3h})=f(w_{3h})-B_h(\zeta_3,w_{3h}).\tag{3.5}$$

Proof. Let $w_{3h}=\zeta_{3h}-\eta_{3h}$, and we have

$$\begin{aligned}\alpha_0\|w_{3h}\|_h^2 \le & B_h(w_{3h},w_{3h})=B_h(\zeta_{3h},w_{3h})-B_h(\eta_{3h},w_{3h})\\ =&B_h(\zeta_3-\eta_{3h},w_{3h})+E_h(\zeta_3,w_{3h}),\end{aligned}$$

which lead to for $w_{3h}\neq 0$,

$$\begin{aligned}\alpha_0\|w_{3h}\|_h \le & \alpha_1\|\zeta_3-\eta_{3h}\|_h+\frac{|E_h(\zeta_3,w_{3h})|}{\|w_{3h}\|_h}\\ \le & \alpha_1\|\zeta_3-\eta_{3h}\|_h+\sup_{w_{3h}\in V_{h3}}\frac{|E_h(\zeta_3,w_{3h})|}{\|w_{3h}\|_h}.\end{aligned}$$

Note that $\|\zeta_3-\zeta_{3h}\|_h\le\|\zeta_3-\eta_{3h}\|_h+\|w_{3h}\|_h$, and we get

$$\|\zeta_3-\zeta_{3h}\|_h\le\left(1+\frac{\alpha_1}{\alpha_0}\right)\|\zeta_3-\eta_{3h}\|_h+\frac{1}{\alpha_0}\sup_{w_{3h}\in V_{h3}}\frac{|E_h(\zeta_3,w_{3h})|}{\|w_{3h}\|_h},$$

which leads to the desired result of (3.4). The proof is completed. □

Lemma 3.3 (Consistency error estimate)**.** *Suppose that the solution $\zeta_3\in H^2(\omega)\cap H^3(\omega)$. Then,*

(I) for C^0 nonconforming elements: Zienkiewicz, Specht and ACM element, if w_{3h} satisfies the conditions C1), C2), C3) and C5), it holds

$$|E_h(\zeta_3,w_{3h})|\le Ch|\zeta_3|_{3,\omega}\|w_{3h}\|_h, \tag{3.6}$$

(II) for non C^0 nonconforming elements: Morley, Fraeijs de Veubeke and rectangular Morley element, if w_{3h} satisfies the conditions C1), C4) and C5), there holds

$$|E_h(\zeta_3,w_{3h})|\le Ch(|\zeta_3|_{3,\omega}+h\|f\|_{0,\omega})\|w_{3h}\|_h. \tag{3.7}$$

Proof. We now start to prove (3.6). In fact, by Green's formula and (3.5), we get

$$\begin{aligned}E_h(\zeta_3,w_{3h})=&\sum_{T\in\mathcal{T}_h}\int_T(p_3w_{3h}-s_\alpha\partial_\alpha w_{3h})dx+\sum_{T\in\mathcal{T}_h}\int_T m_{\alpha\beta}\partial_{\alpha\beta}w_{3h}dx-\sum_{T\in\mathcal{T}_h}\int_T n^\theta_{\alpha\beta}\partial_\alpha\theta\partial_\beta w_{3h}dx\\ =&\sum_{T\in\mathcal{T}_h}\int_T(p_3w_{3h}-s_\alpha\partial_\alpha w_{3h})dx+\sum_{\partial T\in\mathcal{T}_h}\int_{\partial T}m_{\alpha\beta}\partial_\beta w_{3h}\nu_\alpha ds\\ &-\sum_{T\in\mathcal{T}_h}\int_T(\partial_\alpha m_{\alpha\beta}+n^\theta_{\alpha\beta}\partial_\alpha\theta)\partial_\beta w_{3h}dx\\ \le&\sum_{T\in\mathcal{T}_h}\int_T(p_3-s_\alpha-\partial_\alpha m_{\alpha\beta}-n^\theta_{\alpha\beta}\partial_\alpha\theta)\partial_\beta w_{3h}dx+\sum_{\partial T\in\mathcal{T}_h}\int_{\partial T}m_{\alpha\beta}\partial_\beta w_{3h}\nu_\alpha ds,\end{aligned} \tag{3.8}$$

where

$$\left|\sum_{T\in\mathcal{T}_h}\int_T(p_3-s_\alpha-\partial_\alpha m_{\alpha\beta}-n^\theta_{\alpha\beta}\partial_\alpha\theta)\partial_\beta w_{3h}dx\right|\leq Ch|\zeta_3|_{3,\omega}\|w_{3h}\|_h.$$

Since $w_{3h}\in V_{3h}\in C^0(\omega)$, and from conditions C1), C2), C3) and C5) we have

$$|E_h(\zeta_3,w_{3h})|\leq\left|\sum_{\partial T\in\mathcal{T}_h}\int_{\partial T}m_{\alpha\beta}\partial_\beta w_{3h}\nu_\alpha ds\right|\leq Ch|\zeta_3|_{3,\omega}\|w_{3h}\|_h.$$

(II) Since $V_{3h}\not\subset C^0(\omega)$ implies $V_{3h}\not\subset H^1(\omega)$, we modify the expression (3.8) as follows. Let w^I_{3h} be the continuous piecewise linear or bilinear interpolation of w_{3h}. Then $w^I_{3h}\subset C^0(\omega)$, which leads to

$$\begin{aligned}B_h(\zeta_3,w_{3h})=&-\sum_T\int_T m_{\alpha\beta}\partial_{\alpha\beta}w^I_{3h}dx+\sum_T\int_T n^\theta_{\alpha\beta}\partial_\alpha\theta\partial_\beta w^I_{3h}dx\\&-\sum_T\int_T m_{\alpha\beta}\partial_{\alpha\beta}(w_{3h}-w^I_{3h})dx+\sum_T\int_T n^\theta_{\alpha\beta}\partial_\alpha\theta\partial_\beta(w_{3h}-w^I_{3h})dx\\=&f(w^I_{3h})-\sum_T\int_T m_{\alpha\beta}\partial_{\alpha\beta}(w_{3h}-w^I_{3h})dx+\sum_T\int_T n^\theta_{\alpha\beta}\partial_\alpha\theta\partial_\beta(w_{3h}-w^I_{3h})dx\\=&f(w^I_{3h})+\sum_T\int_T(\partial_\alpha m_{\alpha\beta}+n^\theta_{\alpha\beta}\partial_\alpha\theta)\partial_\beta(w_{3h}-w^I_{3h})dx-\sum_T\int_{\partial T}m_{\alpha\beta}\partial_\beta(w_{3h}-w^I_{3h})\nu_\alpha ds.\end{aligned}$$

Thus, we have

$$\begin{aligned}E_h(\zeta_3,w_{3h})=&f(w_{3h}-w^I_{3h})-\sum_T\int_T(m_{\alpha\beta}+n^\theta_{\alpha\beta}\partial_\alpha\theta)\partial_\beta(w_{3h}-w^I_{3h})dx\\&+\sum_{\partial T\in\mathcal{T}_h}\int_{\partial T}m_{\alpha\beta}\partial_\beta(w_{3h}-w^I_{3h})\nu_\alpha ds\\=&E^1_h-E^2_h+E^3_h.\end{aligned}$$

For E^1_h, by the interpolation theorem, we have

$$E^1_h\leq\|f\|_{0,\omega}\|w_{3h}-w^I_{3h}\|_{0,\omega}\leq Ch^2||f||_{0,\omega}\|w_{3h}\|_h.$$

For E^2_h, by the Cauchy-Schwarz inequality, it can be estimated as

$$E^2_h\leq Ch|\zeta_3|_{3,\omega}\|w_{3h}\|_h.$$

For E^3_h, from condition C4), we have

$$\int_F\left[\frac{\partial(w_{3h}-w^I_{3h})}{\partial\nu}\right]ds=0,$$

where

$$[\partial_\beta w_{3h}]|_F := \partial_\beta w_{3h}|_{T_+} - \partial_\beta w_{3h}|_{T_-}, \qquad F \subset \partial T \cap \partial\omega = \emptyset,$$
$$[\partial_\beta w_{3h}]|_F := \partial_\beta w_{3h}|_T, \qquad F \subset \partial T \cap \partial\omega = \gamma_0.$$

Then by the Cauchy-Schwarz inequality, trace theorem [36], inverse inequality (Theorems 6.5-2 and 6.8-1 of [37]), Poincaré-Friedrichs inequality [38] and the condition C5), we obtain

$$\begin{aligned}
&\sum_{\partial T}\sum_{F\in\partial T}\int_F (m_{\alpha\beta} - P_0^F(m_{\alpha\beta}))[\partial_\beta(w_{3h} - w_{3h}^I)]_F \nu_\alpha ds \\
\leq& \left(\|m_{\alpha\beta} - P_0^F(m_{\alpha\beta})\|_{0,F}\right)\left(\|\partial_\beta w_{3h}\nu_\alpha\|_{0,F}\right) \\
\leq& Ch|\zeta_3|_{3,\omega}\|w_{3h}\|_h,
\end{aligned}$$

where

$$P_0^F(m_{\alpha\beta}) = \frac{1}{|F|}\int_F m_{\alpha\beta} ds, \quad ||\cdot||_{0,F} = \left(\int_F |\cdot|^2 ds\right)^{1/2}, \quad \forall F \in \partial T.$$

Finally, we deduce that

$$|E_h(\zeta_3, w_{3h})| \leq Ch(|\zeta_3| + h\|f\|_{0,\omega})\|w_{3h}\|_h.$$

This completes the proof. □

Based on the above lemmas, we have the following main result:

Theorem 3.1 (Existence, uniqueness and convergence of the discrete solution)**.** *Let the assumptions in Theorem* 2.1 *hold. Then, the variational problem* (3.1) *has a unique solution. Let* $\vec{\zeta}$ *and* $\vec{\zeta}_h$ *be the solutions to problems* (2.2) *and* (3.1)*, respectively. Then, we have*

$$\|\vec{\zeta} - \vec{\zeta}_h\| \leq Ch\left(\sum_\alpha |\zeta_\alpha|_2^2 + |\zeta_3|_3^2\right)^{1/2}. \tag{3.9}$$

Proof. First, according to Lemma 3.1, the bilinear form $B_h(\cdot,\cdot)$ has continuity and coercivity over the space $\vec{V}_h$. Judging from the Lax-Milgram theorem, the discrete problem (3.1) has a unique solution (cf. e.g., [19]).

Next, we prove the error estimate of (3.9). It is divided into two cases.

Case 1. For conforming finite elements, define the interpolation operator $\Pi_h : C^0(\omega) \times C^0(\omega) \to V_{\alpha h}$ as

$$\Pi_h \vec{\zeta}_H = (\Pi_{1h}\zeta_1, \Pi_{2h}\zeta_2), \quad \forall \vec{\zeta}_H \in C^0(\omega) \times C^0(\omega).$$

From the interpolation theorem, we have

$$\begin{aligned}
\|\zeta_\alpha - \zeta_{\alpha h}\|_{H^1} &\leq \inf_{\eta_{\alpha h}\in V_{\alpha h}} \|\zeta_\alpha - \eta_{\alpha h}\|_{H^1} \\
&\leq Ch|\zeta_\alpha|_{2,\omega}, \quad (\alpha = 1,2), \quad \forall \zeta_\alpha \in H^2(\omega).
\end{aligned} \tag{3.10}$$

Case 2. For nonconforming finite elements, define the interpolation operator $\Pi_h: H^2(\omega) \to V_{3h}$ as

$$\Pi_h \zeta_3 = (\Pi_{3h} \zeta_3), \quad \forall \zeta_3 \in C^0(\omega).$$

Then, we have

$$\begin{aligned} \|\zeta_3 - \zeta_{3h}\|_h &\leq \inf_{\eta_{3h} \in V_{3h}} \|\zeta_3 - \eta_{3h}\| \leq \|\zeta_3 - \Pi_{3h}\eta_{3h}\| \\ &\leq Ch|\zeta_3|_{3,\omega}, \quad \forall \zeta_3 \in H^3(\omega), \end{aligned}$$

which together with the conclusion of (3.4) (Strang lemma) and Lemma 3.3 yields

$$\|\zeta_3 - \zeta_{3h}\|_h \leq Ch|\zeta_3|_{3,\omega} \quad \text{or} \quad \|\zeta_3 - \zeta_{3h}\|_h \leq Ch(|\zeta_3|_{3,\omega} + h\|f\|_{0,\omega}), \quad \forall \zeta_3 \in H^3(\omega). \tag{3.11}$$

Finally, combine (3.10) and (3.11) to get

$$\begin{aligned} \|\vec{\zeta} - \vec{\zeta}_h\| &= \left(\sum_\alpha \|\zeta_\alpha - \zeta_{\alpha h}\|_{H^1}^2 + \|\zeta_3 - \zeta_{3h}\|_h^2 \right)^{1/2} \\ &\leq Ch \left(\sum_\alpha |\zeta_\alpha|_2^2 + |\zeta_3|_3^2 \right)^{1/2}. \end{aligned}$$

The proof is completed. □

4 Numerical examples

In this section, we mainly conduct numerical experiments on paraboloid, spherical dome and cylindrical bridge, and analyze their numerical results.

4.1 Paraboloid

In the Cartesian coordinate system, the equation of the any point (x_1, x_2) on the paraboloid S is as follows:

$$\theta = \theta(x_1, x_2) = \frac{x_1^2}{2} + \frac{x_2^2}{2}.$$

The integral domain ω on S is defined by

$$\omega := \left\{ (x_1, x_2) \in \mathbb{R}^2;\ x_1^2 + x_2^2 \leq 1 \right\},$$

and $\gamma_0 = \partial\omega$ is the totally clamped boundary.

According to [39], we take the values of the Young's modulus E and the Poisson ratio ν as

$$E = 1 \times 10^7 \text{Pa}, \quad \nu = 0.3. \tag{4.1}$$

Table 1: Numerical results for paraboloid on four different meshes.

Extremum	Mesh steps				Reference solution
	1/40	1/80	1/160	1/320	
$\zeta_{1\max}$	6.1958e-8	6.1062e-8	6.0564e-8	6.0391e-8	6.0366e-8
$\zeta_{1\min}$	-6.3397e-8	-6.1242e-8	-6.0502e-8	-6.0393e-8	-6.0365e-8
$\zeta_{2\max}$	6.2954e-8	6.0678e-8	6.0156e-8	6.0069e-8	6.0034e-8
$\zeta_{2\min}$	-6.2952e-8	-6.0810e-8	-6.0731e-8	-6.0565e-8	-6.0537e-8
$\zeta_{3\max}$	4.3446e-7	4.1393e-7	4.0747e-7	4.0600e-7	4.0554e-7
$\zeta_{3\min}$	-1.3748e-7	-6.4401e-8	-3.7925e-8	-1.9733e-8	-0.6341e-8

The Lamé constants ($\lambda \geq 0$, $\mu > 0$) can be derived from the following equations (cf. [39]):

$$\lambda = \frac{E\nu}{(1+\nu)(1-2\nu)}, \quad \mu = \frac{E}{2(1+\nu)}. \tag{4.2}$$

Plugging (4.1) into (4.2), we yield

$$\lambda = 5.77 \times 10^6 \text{Pa}, \quad \mu = 3.85 \times 10^6 \text{Pa}.$$

Suppose the applied force at the paraboloid to be $p_1 = p_2 = 0$, and $p_3 = 200$Pa. We apply the 2D linearly elastic shallow shell model to the paraboloid. The results are shown in Fig. 8, with its left part (cf. A1, B1, C1, D1) representing the grid of 40, 80, 160 and 320 respectively, and the right part (cf. A2, B2, C2, D2) representing the displacement deformation of the four different grids on the middle surface. From A2, B2, C2, D2 in Fig. 8, we could see that the deformation is getting increasingly small from the top to bottom. The blue bottom in each sub-picture indicates that γ_0 portion of the boundary is fixed. The biggest deformation occurs on the top as illustrated in red. As expected, the 2D linearly elastic shallow shell model is relatively stable, i.e., when the grid becomes smaller, the deformation remains independent of its size.

In order to further analyze the numerical results, we compute the maximal values and minimal values of the three components of displacement on different meshes, as shown in Table 1. Since the exact solution cannot be obtained directly, we choose the result under the extremely fine mesh (1000) as the exact solution. Then we derive the errors and convergence orders of the numerical scheme (cf. [40]). As presented in Table 2, we compute the absolute error and the convergence order under the $\vec{L}^2$ norm, the $\vec{H}^1$ norm, and the $H^1 \times H^1 \times H^2$ norm, respectively. It is obvious that when the mesh step becomes smaller, the absolute error also tends to be smaller. The results show that the finite element numerical scheme for the proposed 2D shallow shell model is stable and convergent.

In Table 1, $\zeta_{i\max}$ $(i=1,2,3)$ signifies the maximal value of the components of displacement, and $\zeta_{i\min}$ $(i=1,2,3)$ is the minimal value.

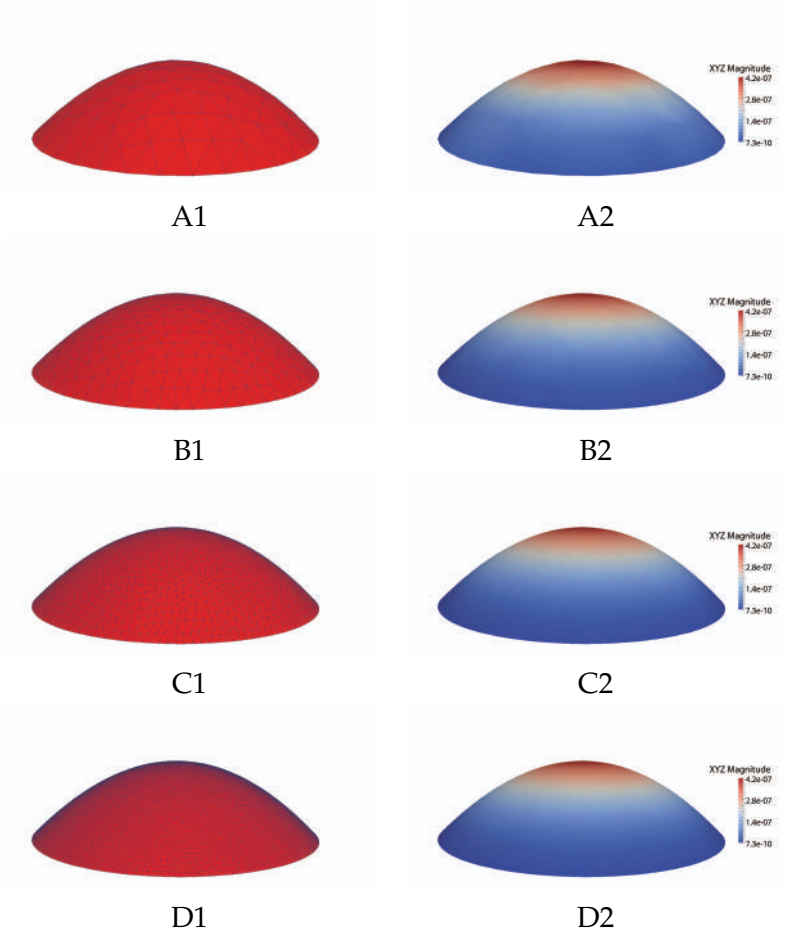

Figure 8: Numerical results for the paraboloid on four different meshes: A1, B1, C1 and D1 denote the mesh of 40, 80, 160 and 320, respectively; A2, B2, C2 and D2 denote the deformation of the corresponding displacement.

4.2 Spherical dome

The equation for the spherical dome (cf. [41]) S at the point (x_1,x_2) is as follows:

$$\theta=\theta(x_1,x_2)=\sqrt{7^2-x_1^2-x_2^2}.$$

The domain ω on S is defined by

$$\omega:=\left\{(x_1,x_2)\in\mathbb{R}^2;\ \left[-5\sqrt{2}/2,5\sqrt{2}/2\right]\times\left[0,\sqrt{5^2-x_1^2}\right]\right\}.$$

And

$$\gamma_0:=\left\{(x_1,x_2)\in\mathbb{R}^2;\ x_1\in\left[-5\sqrt{2}/2,5\sqrt{2}/2\right],\ x_2=\sqrt{5^2-x_1^2}\right\}$$

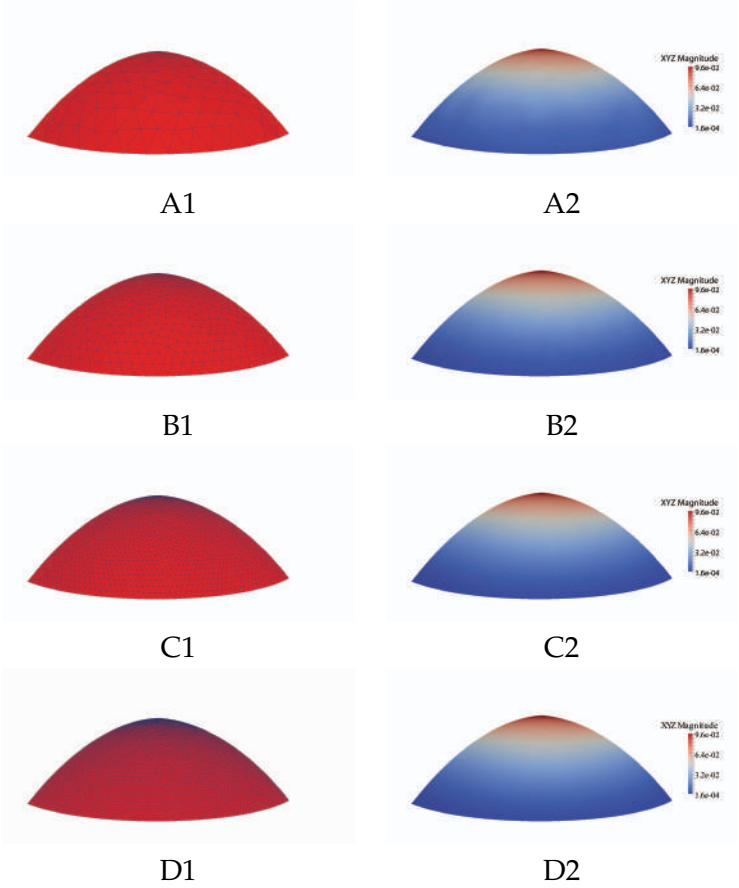

Figure 9: Numerical results for the spherical dome on four different meshes: A1, B1, C1 and D1 denote the mesh of $10\times14\times10$, $20\times28\times20$, $40\times56\times40$ and $80\times112\times80$, respectively; A2, B2, C2 and D2 denote the deformation of the corresponding displacement.

is the clamped boundary, whereas

$$\gamma_1 := \left\{ (x_1,x_2)\in\mathbb{R}^2;\ x_1=\pm x_2,\ x_2\in\left[0,5\sqrt{2}/2\right] \right\}$$

is the free boundary.

The values of Young's modulus E, Poisson's ratio ν and the force applied to the spherical dome are the same as in Subsection 4.1. The results are depicted in Fig. 9, with its the left part (cf. A1, B1, C1, D1) representing the grid of $10\times14\times10$, $20\times28\times20$, $40\times56\times40$ and $80\times112\times80$ respectively, and the right part (cf. A2, B2, C2, D2) representing the displacement deformation of the four different grids on the middle surface.

Similar to Subsection 4.1, we compute the maximal values and minimal values of the three components of displacement on different meshes, as shown in Table 3. Since the exact solution cannot be obtained directly, we choose the result under the extremely fine mesh ($250\times350\times250$) as the exact solution. As presented in Table 4, we compute

Table 2: Error and rate of convergence for paraboloid on four different meshes.

Mesh steps	1/40	1/80	1/160	1/320
$\|\cdot\|_{L^2\times L^2\times L^2 error}$	4.6088e-8	1.1546e-8	2.7031e-9	6.4713e-10
Rate of convergence	1.997	2.095	2.062	\
$\|\cdot\|_{H^1\times H^1\times H^1 error}$	2.2657e-7	9.4994e-8	4.1100e-8	2.0269e-8
Rate of convergence	1.254	1.209	1.020	\
$\|\cdot\|_{H^1\times H^1\times H^2 error}$	1.6475e-6	8.3289e-7	4.1313e-7	2.1735e-7
Rate of convergence	0.984	1.012	0.927	\

Table 3: Numerical results for spherical dome on four different meshes.

Extremum	Mesh steps				Reference solution
	1/14	1/28	1/56	1/112	
$\zeta_{1\max}$	1.9005e-3	2.0490e-3	2.1975e-3	2.2597e-3	2.2785e-3
$\zeta_{1\min}$	-1.8972e-3	-2.0500e-3	-2.1716e-3	-2.2584e-3	-2.2789e-3
$\zeta_{2\max}$	3.9192e-2	4.0479e-2	4.0756e-2	4.0824e-2	4.0841e-2
$\zeta_{2\min}$	-2.1911e-3	-1.9208e-3	-7.2610e-4	-1.4253e-4	-1.6052e-4
$\zeta_{3\max}$	9.0987e-2	9.3677e-2	9.4233e-2	9.4372e-2	9.4408e-2
$\zeta_{3\min}$	-8.6706e-3	-7.6401e-3	-3.9221e-3	-1.7993e-3	-7.1990e-4

Table 4: Error and rate of convergence for spherical dome on four different meshes.

mesh steps	1/14	1/28	1/56	1/112
$\|\cdot\|_{L^2\times L^2\times L^2 error}$	9.5332e-3	2.1688e-3	5.5079e-4	1.2175e-4
Rate of convergence	2.136	1.977	2.177	\
$\|\cdot\|_{H^1\times H^1\times H^1 error}$	2.0046e-2	7.7522e-3	3.6803e-3	1.7456e-3
Rate of convergence	1.371	1.075	1.076	\
$\|\cdot\|_{H^1\times H^1\times H^2 error}$	4.0072e-2	1.9609e-2	1.0188e-2	5.2692e-3
Rate of convergence	1.031	0.945	0.951	\

the absolute error and the convergence order under the $\vec{L}^2$ norm, the $\vec{H}^1$ norm, and the $H^1\times H^1\times H^2$ norm, respectively.

4.3 Cylindrical bridge

We use a portion of the cylindrical surface [42] to represent the geometry of main arch bridge (Fig. 10). In the rectangular coordinate system, the equation of the cylindrical surface (generatrix is parallel to the O-xy plane) is as follows:

$$\theta=\theta(x_1,x_2)=\sqrt{5^2-x_1^2}.$$

The domain ω on S is defined by

$$\omega:=\left\{(x_1,x_2)\in\mathbb{R}^2;\ -\pi\le x_1\le\pi,\ -1\le x_2\le 1\right\}.$$

Figure 10: Krk bridge, Yugoslavia.

And

$$\gamma_0 := \{(x_1,x_2) \in \mathbb{R}^2;\ x_1 = -\pi \text{ and } x_1 = \pi,\ x_2 \in [-1,1]\}$$

is the clamped boundary, whereas

$$\gamma_1 := \{(x_1,x_2) \in \mathbb{R}^2;\ x_1 \in [-\pi,\pi],\ x_2 = -1 \text{ and } x_2 = 1\}$$

is the free boundary.

The value of Young's modulus E is 3.45×10^{10} Pa and Poisson's ratio ν is 0.2 (cf. [42]). The force applied to the cylindrical bridge is the same as in Subsection 4.1. The deformation results are shown in Fig. 11.

Similarly, we compute the maximal values and minimal values of the three components of displacement on different meshes, as displayed in Table 5. Since the exact solution cannot be obtained directly, we choose the result under the extremely fine mesh (570×190) as the exact solution. As illustrated in Table 6, we compute the absolute error and the convergence order under the $\vec{L}^2$ norm, the $\vec{H}^1$ norm, and the $H^1\times H^1\times H^2$ norm, respectively.

To summarize, under the error of the $L^2\times L^2\times L^2$ norm, the convergence rates of paraboloid, spherical dome and cylindrical bridge at different grid steps are approximately second order. This can be found in Fig. 12. Under the error of the $H^1\times H^1\times H^1$ norm and $H^1\times H^1\times H^2$ norm, the convergence rates of paraboloid, spherical dome and

Table 5: Numerical results for cylindrical bridge on four different meshes.

Extremum	Mesh steps				Reference solution
	1/36	1/72	1/144	1/288	
$\zeta_{1\max}$	3.1626e-9	3.1389e-9	3.1361e-9	3.1341e-9	3.1336e-9
$\zeta_{1\min}$	-3.1603e-9	-3.1384e-9	-3.1359e-9	-3.1341e-9	-3.1336e-9
$\zeta_{2\max}$	1.0319e-9	9.1995e-10	8.9236e-10	8.8556e-10	8.8388e-10
$\zeta_{2\min}$	-4.3416e-10	-4.7781e-10	-4.8967e-10	-4.9281e-10	-4.9364e-10
$\zeta_{3\max}$	2.9686e-8	2.9395e-8	2.9317e-8	2.9297e-8	2.9292e-8
$\zeta_{3\min}$	-2.6741e-9	-1.3393e-9	-6.7058e-10	-3.3559e-10	-1.6965e-10

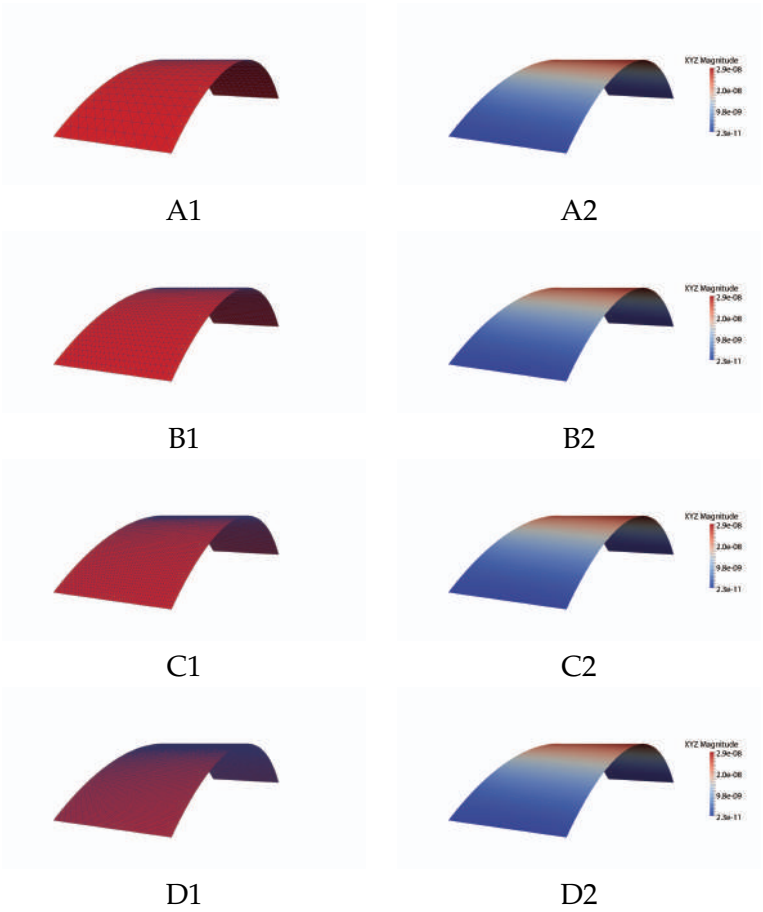

Figure 11: Numerical results for the cylindrical bridge on four different meshes: The left part (A1, B1, C1, D1) denotes the meshing of 36×12, 72×24, 144×48 and 288×96, respectively; The right part (A2, B2, C2, D2) denotes the deformation of the corresponding displacement.

cylindrical bridge at different grid steps are nearly linear, which can be found in Fig. 13 and Fig. 14. The numerical results of the convergence order further validate the results of Theorem 3.1.

Table 6: Error and rate of convergence for cylindrical bridge on four different meshes.

Mesh steps	1/36	1/72	1/144	1/288
$\|\cdot\|_{L^2\times L^2\times L^2 error}$	1.2680e-10	3.2570e-10	7.9757e-11	1.6263e-11
Rate of convergence	1.9610	2.0210	2.2941	\
$\|\cdot\|_{H^1\times H^1\times H^1 error}$	2.4648e-9	9.4351e-10	3.9201e-10	1.8588e-10
Rate of convergence	1.3853	1.2671	1.0765	\
$\|\cdot\|_{H^1\times H^1\times H^2 error}$	7.9593e-9	4.0735e-9	2.0414e-9	1.1173e-9
Rate of convergence	0.9664	0.9967	0.8696	\

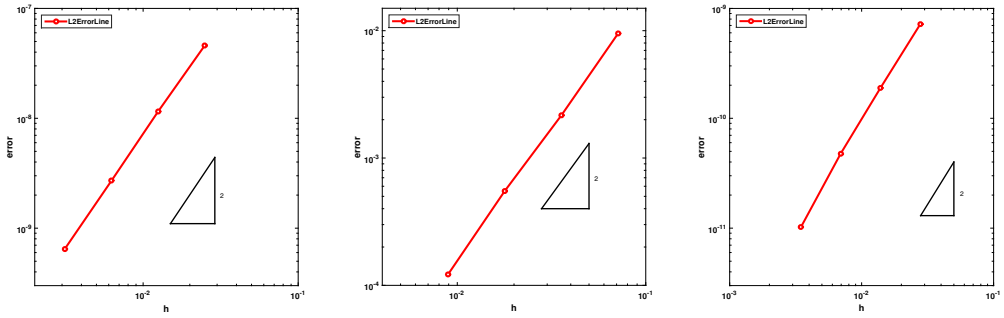

(a) Paraboloid (b) Spherical dome (c) Cylindrical bridge

Figure 12: Rate of convergence with $\|\cdot\|_{L^2\times L^2\times L^2}error\cdot$

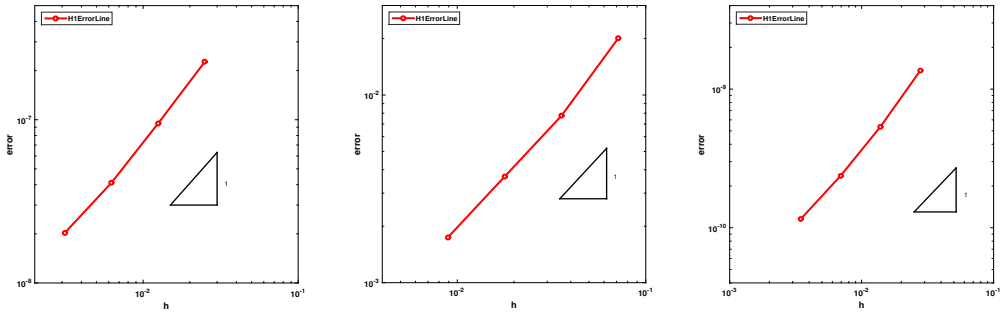

(a) Paraboloid (b) Spherical dome (c) Cylindrical bridge

Figure 13: Rate of convergence with $\|\cdot\|_{H^1\times H^1\times H^1}error\cdot$

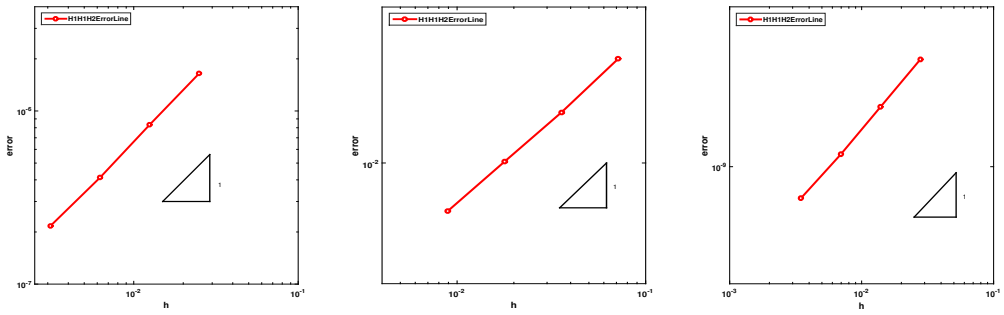

(a) Paraboloid (b) Spherical dome (c) Cylindrical bridge

Figure 14: Rate of convergence with $\|\cdot\|_{H^1\times H^1\times H^2}error\cdot$

Table 7: Comparison of CPU for two models.

Models	Meshes				The fine mesh
	36×12	72×24	144×48	288×96	
Shallow shell model	1.322s	2.427s	7.078s	29.399s	152.953s
Koiter's model	2.308s	6.264s	23.171s	90.952s	382.696s

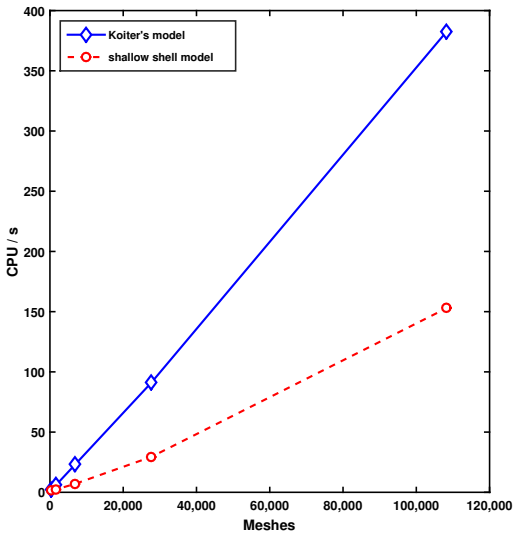

Figure 15: CPU of shallow shell and Koiter's models.

Besides, we also compare the computation time of the shallow shell model with that of the classic Koiter's model [43] under the same meshes, see Table 7. It clearly show that the shallow shell model greatly improves the calculation time in Fig. 15.

5 Conclusions

In this paper, we have provided a series of robust numerical schemes (linear/Morley, Zienkiewicz, Fraeijs de Veubeke, Specht element pair; Bilinear/Rectangular Morley, ACM element pair) to discretize the 2D linearly elastic shallow shell model, and offered a rigorous proof of the existence, uniqueness as well as error estimate of numerical solutions. The numerical simulation results show that our numerical method is stable and convergent. Based on the above results, we can extend our research to engineering fields in the future.

Acknowledgements

This paper is supported by the National Natural Science Foundation of China (NSFC Nos. 11971379 and 12071443) and the Distinguished Youth Foundation of Shaanxi Province (2022JC-01). Part of the work was done during X. Shen's visiting to State Key Laboratory of Scientific and Engineering Computing, Chinese Academy of Sciences. X. Shen appreciates its hospitality. All authors are very grateful to Prof. P. G. Ciarlet's direction and advice.

References

[1] Z. M. ZHANG, *Locking and robustness in the finite element method for circular arch problem,* Numer. Math., 69(4) (1995), pp. 509–522.
[2] A. H. NIEMI, *Approximation of shell layers using bilinear elements on anisotropically refined rectangular meshes,* Comput. Methods Appl. Mech. Eng., 197(45) (2008), pp. 3964–3975.
[3] P. G. CIARLET AND B. MIARA, *Justification of the two-dimensional equations of a linearly elastic shallow shell,* Commun. Pure Appl. Math., 45(3) (1992), pp. 327–360.
[4] A. LÉGER AND B. MIARA, *Mathematical justification of the obstacle problem in the case of a shallow shell,* J. Elast., 90(3) (2008), pp. 241–257.
[5] J. RAJA AND N. SABU, *Justification of two dimensional model of shallow shells using Gamma convergence,* Indian J. Pure Appl. Math., 44(3) (2013), pp. 277–295.
[6] X. Q. SHEN, Q. YANG, L. J. LI, Z. M. GAO AND T. T. WANG, *Numerical approximation of the dynamic Koiter's model for the hyperbolic parabolic shell,* Appl. Numer. Math., 150 (2019), pp. 194–205.
[7] X. Q. SHEN, Q. YANG, L. BAI, AND K. T. LI, *Full discretization scheme for the dynamics of elliptic membrane shell model,* Commun. Comput. Phys., 29(1) (2021), pp. 186–210.
[8] X. Q. SHEN, Y. J. XUE, Q. YANG, AND S. F. ZHU, *Finite element method coupling penalty method for flexural shell model,* Adv. Appl. Math. Mech., 14(2) (2022), pp. 365–385.
[9] R. F. WU, X. Q. SHEN, AND J. K. ZHAO, *Conforming finite element methods for two-dimensional linearly elastic shallow shell and clamped plate models,* Appl. Math. Comput., 430 (2022), 127259.
[10] P. PIERSANTI AND X. Q. SHEN, *Numerical methods for static shallow shells lying over an obstacle,* Numer. Algorithms, 85(3) (2020), pp. 623–652.
[11] P. DANUMJAYA, A. K. PANY, AND A. K. PANI, *Morley FEM for the fourth-order nonlinear reaction-diffusion problems,* Comput. Math. Appl., 99 (2021), pp. 229–245.
[12] P. TROUVÉ, *Sur la convergence des méthodes d'éléments finis nonconformes pour des problèmes linéaires de coques minces,* Numer. Math., 57(1) (1990), pp. 481–524.
[13] R. KOUHIA AND R. STENBERG, *A linear nonconforming finite element method for nearly incompressible elasticity and Stokes flow,* Comput. Methods Appl. Mech. Eng., 124(3) (1995), pp. 195–212.
[14] P. B. MING AND Z. C. SHI, *Nonconforming rotated Q_1 element for Reissner-Mindlin plate,* Math. Models Methods Appl. Sci., 11(8) (2001), pp. 1311–1342.
[15] J. DOUGLAS, J. E. SANTOS, AND D. SHEEN, *A nonconforming mixed finite element method for Maxwell's equations,* Math. Models Methods Appl. Sci., 10(04) (2000), pp. 593–613.
[16] P. G. CIARLET, Mathematical Elasticity, Vol. III. Theory of Shells, North-Holland, Amsterdam, 2000.

[17] E. VENTSEL AND T. KRAUTHAMMER, Thin Plates and Shells: Theory, Analysis, and Applications, CRC Press, Boca Raton, 2001.
[18] P. G. CIARLET, Mathematical Elasticity, Vol. II. Theory of Plates, North-Holland, Amsterdam, 1997.
[19] L. C. EVANS, Partial Differential Equations, American Mathematical Society, Providence, 2010.
[20] H. R. CHEN, S. C. CHEN, AND Z. H. QIAO, *C^0-nonconforming tetrahedral and cuboid elements for the three-dimensional fourth order elliptic problem,* Numer. Math., 124(1) (2013), pp. 99–119.
[21] A. DJURDJEVAC, C. M. ELLIOTT, R. KORNHUBER, AND T. RANNER, *Evolving surface finite element methods for random advection-diffusion equations,* SIAM/ASA J. Uncertain. Quantif., 6(4) (2018), pp. 1656–1684.
[22] E. SÜLI AND T. TSCHERPEL, *Fully discrete finite element approximation of unsteady flows of implicitly constituted incompressible fluids,* IMA J. Numer. Anal., 40(2) (2020), pp. 801–849.
[23] P. G. CIARLET, The Finite Element Method for Elliptic Problems, Society for Industrial and Applied Mathematics, Philadelphia, 2002.
[24] L. S. D. MORLEY, *The triangular equilibrium element in the solution of plate bending problems,* Aero. Quart., 19(2) (1968), pp. 149–169.
[25] G. P. BAZELEY, Y. K. CHEUNG, B. M. IRONS, AND O. C. ZIENKIEWICZ, *Triangular elements in bending-conforming and nonconforming solutions,* in Proceedings of the Conference on Matrix Methods in Structural Mechanic, pages 547–579. Wright Patterson Air Force Bases, Ohio, 1965.
[26] P. LASCAUX AND P. LESAINT, *Some nonconforming finite elements for the plate bending problem,* RAIRO Anal. Numér., 9(1) (1975), pp. 9–53.
[27] H. L. LI, P. B. MING, AND Z. C. SHI, *The quadratic Specht triangle,* J. Comput. Math., 38(1) (2020), pp. 103–124.
[28] B. SPECHT, *Modified shape functions for the three-node plate bending element passing the patch test,* Int. J. Numer. Methods Eng., 26(3) (1988), pp. 705–715.
[29] D. Y. SHI AND P. L. XIE, *Morley type non C^0 nonconforming rectangular plate finite elements on anisotropic meshes,* Numer. Methods Partial Differential Equations, 26(3) (2010), pp. 723–744.
[30] M. WANG, Z. C. SHI, AND J. C. XU, *Some n-rectangle nonconforming elements for fourth order elliptic equations,* J. Comput. Math., 25(4) (2007), pp. 408–420.
[31] D. Y. SHI, S. P. MAO, AND S. C. CHEN, *On the anisotropic accuracy analysis of ACM's nonconforming finite element,* J. Comput. Math., 23(6) (2005), pp. 635–646.
[32] F. STUMMEL, *Basic compactness properties of nonconforming and hybrid finite element spaces,* RAIRO Anal. Numér., 41(1) (1980), pp. 81–115.
[33] P. G. CIARLET, Y. F. HOU, AND C. MARDARE, *On Korn's inequalities on a surface,* Anal. Appl., 14(3) (2016), pp. 415–447.
[34] H. L. LI, P. B. MING, AND Z. C. SHI, *Two robust nonconforming H^2- elements for linear strain gradient elasticity,* Numer. Math., 137 (2016), pp. 691–711.
[35] M. WANG, *The generalized Korn inequalities on nonconforming finite element spaces,* Math. Numer. Sin., 16(1) (1994), pp. 108–113.
[36] S. C. BRENNER AND L. R. SCOTT, The Mathematical Theory of Finite Element Methods, Springer, New York, 2008.
[37] P. G. CIARLET, Linear and Nonlinear Functional Analysis with Applications, Society for Industrial and Applied Mathematics, Philadelphia, 2013.
[38] H. L. GUO, Z. M ZHANG, AND Q. S. ZOU, *A C^0 linear finite element method for biharmonic problems,* J. Sci. Comput., 74(3) (2017), pp. 1–26.

[39] B. H. SUN, W. ZHANG, K. Y. YEH, AND F. P. J. RIMROTT, *Exact displacement solution of arbitrary degree paraboloidal shallow shell of revolution made of linear elastic materials,* Int. J. Solids Struct., 33(16) (1996), pp. 2299–2308.
[40] X. Q. SHEN, J. J. JIA, S. F. ZHU, H. M. LI, L. BAI, T. T. WANG, AND X. S. CAO, *The time-dependent generalized membrane shell model and its numerical computation,* Comput. Methods Appl. Mech. Eng., 344 (2019), pp. 54–70.
[41] A. H. NIEMI, *Benchmark computations of stresses in a spherical dome with shell finite elements,* SIAM J. Sci. Comput., 38(3) (2016), pp. 440–457.
[42] I. STOJADINOVIC, *The design of the mianland-island Krk bridge,* Gradev., 33(2) (1981), pp. 25–75.
[43] X. Q. SHEN AND H. M. LI, *The time-dependent Koiter model and its numerical computation,* Appl. Math. Model., 55 (2018), pp. 131–144.